Catalysis Today 178 (2011) 12–24

Contents lists available at SciVerse ScienceDirect

Catalysis Today

journal homepage: www.elsevier.com/locate/cattod

Partial oxidation of methane to synthesis gas on $Rh/Zr_xCe_{1-x}O_2–Al_2O_3$

Sara Boullosa-Eiras, Tiejun Zhao, Estelle Vanhaecke, De Chen, Anders Holmen*

Department of Chemical Engineering, Norwegian University of Science and Technology, Sem Sælands vei 4, NO-7491 Trondheim, Norway

ARTICLE INFO

Article history:
Received 29 April 2011
Received in revised form 10 August 2011
Accepted 14 August 2011
Available online 21 September 2011

Keywords:
Methane partial oxidation
Rhodium
Ceria
Zirconia
Alumina

ABSTRACT

A series of $Zr_xCe_{1-x}O_2–Al_2O_3$ ($x = 0$, 0.25, 0.5, 1) nanocomposites were prepared through a citric acid mediated route. The thermal stability of these materials was investigated by calcination at temperatures between 1173 and 1473 K for a certain time. The nanocomposites were characterized by XRD, DTA, nitrogen adsorption–desorption measurements, Raman spectroscopy, TEM and SEM. It was found that coating $Zr_xCe_{1-x}O_2$ on the surface of Al_2O_3 could substantially enhance the thermal stability of the composites, as evidenced by preventing the formation of α-Al_2O_3. $Rh/Zr_xCe_{1-x}O_2–Al_2O_3$ catalysts were prepared by incipient wetness impregnation, followed by calcination at 1173 K for 5 h. The Rh dispersion was measured by volumetric H_2-chemisorption. The effect of the catalyst support, the reaction temperature, the Rh loading and the gas hourly space velocity in the catalytic partial oxidation of methane was studied in a quartz fixed-bed reactor, concerning activity, selectivity and stability. The ignition and extinction behaviors of the reactor on different catalysts were also investigated showing that the ignition temperature depends significantly on the composition of the supports. It was observed that the presence of cerium in the composites would lower the ignition temperature and enhance the activities of methane partial oxidation and water gas shift reaction.

1. Introduction

Catalytic partial oxidation of methane (CPO) is an interesting alternative to the conventional steam methane reforming (SMR) for synthesis gas production. It yields a suitable H_2/CO (about 2) ratio for the synthesis of methanol or dimethyl ether and for the Fischer–Tropsch synthesis [1]. In addition, CPO can be operated in a millisecond contact-time reactor, making the process compact and thus suitable for on-board H_2 production in fuel cell applications [2]. A wide range of catalysts have been found to be active for the CPO process, such as supported Ni [3], Co [4], Pt [5], Rh [6], Ru [7], etc. It has been shown that Rh-based catalysts present the most promising catalytic performance for CPO with high activity and selectivity towards H_2 and CO, and good stability [1]. A good catalytic performance has been achieved for catalyst containing 5 wt.% Rh supported on corundum, showing a good stability and activity [8]. However, Rh is an expensive material and it must be employed efficiently. One feasible route is to prepare high-dispersed Rh nanoparticles on a support with high thermal stability at the operating conditions.

Thermodynamic analysis of the CPO process indicates that elevated temperature is favored for obtaining high conversion and selectivity to H_2 and CO [1]. It has been reported that the reaction temperature of CPO can reach values higher than 1273 K, and more extreme temperatures are expected on the catalyst surface due to the exothermity of CPO and heat transport limitations on the external film of the catalyst [6,9,10]. High temperatures enhance the intrinsically high reaction rate for the CPO process, thus allowing the process to be very compact. However, extremely high temperatures lead to severe sintering of the metal and the oxide supports. For instance, the often used γ-Al_2O_3 supports with a high surface area are gradually transformed into low surface area α-Al_2O_3 when the temperature increases to 1273 K or higher. This transformation to α-Al_2O_3 may lead to the encapsulation of metal particles by closure of pores at high temperatures [11,12]. In addition, α-Al_2O_3 shows poor mechanical properties, giving a higher cracking possibility, especially when the temperature changes rapidly such as during the ignition and extinction periods [13]. Direct use of α-Al_2O_3 foam could reduce the cracking possibility. Nevertheless, the very low surface area and the inert surface of this foam lead to poor dispersion and large particle size of the active metallic phase (hundreds of nanometers). The addition of another oxide such as CeO_2 to form a washcoat has been found to effectively enhance the dispersion of Rh and thus a better catalytic performance [8]. Therefore, developing a suitable support system and thus a catalyst is highly interesting for the CPO process.

Many attempts to produce a highly thermal stable oxide system have been reported during the last decade [5,14–16]. A feasible route is to form a well-organized composite through introducing an extra phase into the parent phase. Thus, effectively

---

* Corresponding author. Tel.: +47 73594151.
E-mail address: anders.holmen@chemeng.ntnu.no (A. Holmen).

0920-5861/$ – see front matter © 2011 Elsevier B.V. All rights reserved.
doi:10.1016/j.cattod.2011.08.029

enhancing the thermal stability of the catalyst support system, and simultaneously improving the stability of the metallic phase to some extend [17,18]. Fornasiero et al. [14,19–22] have studied the $Zr_xCe_{1-x}O_2$–Al_2O_3 system by applying the incipient wetness impregnation of the Ce- and Zr-precursors with citric acid as complexing agent into the parent alumina. They found an enhanced thermal stability of these nanocomposites due to a synergic stabilization between $Zr_xCe_{1-x}O_2$ and Al_2O_3. Subsequently, catalysts prepared with these nanocomposite systems exhibited an excellent catalytic performance in the three-way catalyst as well as for ethanol steam reforming and water gas shift reaction [19,21]. In addition, Hori et al. have investigated the modified alumina doped with ceria, zirconia or mixtures of both [5,23–25] and then, these composite systems were employed to support Pt as a novel catalyst for CPO. The use of the modified support can help to avoid the coke formation and prevent the subsequent deactivation of the Pt catalysts. Due to the complexity of these nanocomposites, the physico-chemical properties of the materials as a function of composite and structures have not been addressed, and a systematic study of these composites is needed [20].

In this article, we address the thermal stability of the $Zr_xCe_{1-x}O_2$–Al_2O_3 nanocomposites and their application in the CPO process. The effects of the composition, the preparation details, and the calcination temperature on the physico-chemical properties of these composites are investigated based on different characterization techniques. The produced composites are used as catalyst support to deposit the Rh metallic phase by the impregnation method. The effect of catalyst support composition, the gas space velocity, the loading of Rh, and the reaction temperature on the catalyst performance of these catalysts are investigated in a quartz fixed-bed for the CPO process.

2. Experimental

2.1. Catalyst preparation

An excessive solvent impregnation method through a simple evaporation-drying procedure was employed for the preparation of 5 wt.% $Zr_xCe_{1-x}O_2$–Al_2O_3 supports. It should be noticed that $Zr_xCe_{1-x}O_2$ in this case is used to express the chemical composition, not for a solid solution. A certain amount of zirconyl nitrate ($ZrO(NO_3)_3 \cdot xH_2O$, 37.5 wt.% ZrO_2), cerium nitrate ($Ce(NO_3)_3 \cdot 6H_2O$) and citric acid ($C_6H_8O_7$) were dissolved into deionized water (95 mL) followed by adding polyethylene glycol (0.1 g/mL) to form a complex solution. Then, the weighed alumina powder (Sasol Puralox 200 SCCa) was added stepwise into the above complex solution under vigorous stirring to produce a suspension. The water in this suspension was evaporated at 358 K for 2 days to form a dried solid. The final powdered composites thus produced were treated in air at temperatures from 1173 to 1473 K for 5 h. For the sake of comparison, $Zr_xCe_{1-x}O_2$ was also prepared by a similar procedure. Further details of the preparation method have been reported elsewhere [26]. For the preparation of the Rh catalyst, rhodium nitrate was impregnated into the $Zr_xCe_{1-x}O_2$–Al_2O_3 support aged at 1173 K for 5 h.

2.2. Catalyst characterization

2.2.1. X-ray diffraction (XRD)

X-ray diffraction (XRD) patterns of these composites were recorded at room temperature on a Bruker AXS D8 Focus diffractometer using Cu Kα radiation ($\lambda = 1.54$ Å). The X-ray tube voltage was set to 40 kV and the current to 50 mA. XRD patterns were collected in the range of 2θ from 20° to 85°, at 0.01°/step with integration times of 1 s/step and 2θ from 27° to 32°, at 0.02°/step with integration times of 10 s/step. Diffractograms were analyzed by employing the TOPAS program applying the Rietveld fitting [27] to estimate the alumina phase composition and the Pawley method [28] to calculate the crystal size of $Zr_xCe_{1-x}O_2$ and Al_2O_3 in these composites.

2.2.2. Differential thermal analysis (DTA)

DTA in an oxidising atmosphere was used to investigate the phase transition of the different supports. DTA was carried out using a Jupiter STA 449C from Netzsch. The samples were heated to 1803 K at a heating rate of 10 K/min in air. The total flow, 80 mL/min air and 20 mL/min argon (protective gas for weighing house), was fed through the sample compartment.

2.2.3. Textual properties

Nitrogen adsorption–desorption isotherms of the samples were measured with a Micromeritics TriStar 3000 instrument, and the data was collected at liquid nitrogen temperature, 77 K. Prior to the measurements, the samples were outgassed at 473 K overnight. The surface area was calculated employing the Brunauer–Emmett–Teller (BET) equation.

2.2.4. Raman spectroscopy

Raman spectra were collected on a Horiba Jobin Yvon LabRAM HR800 spectrometer. The emission lines at 633 nm were focused on the sample with a 100× objective from a He–Ne laser and 325 nm from He–Cd laser were focused on the sample with a 40× NUV objective. UV Raman is particularly appreciated to overcome fluorescence, usually present for alumina powder and to increase the sensitivity especially at the surface [29].

2.2.5. Electron microscopy

Electron micrographs were acquired using a SEM (Hitachi S4300 field emission microscope on a Zeiss Ultra 55-limited edition) and a TEM (JEOL JEM 2010F, operated at 200 kV). For the TEM samples, a suspension of small amount of the sample in ethanol was given an ultrasonic treatment for 1 min and then dropped onto a copper grid covered by a holey carbon film.

2.2.6. H_2-chemisorption

Rh dispersions in the catalysts after heat treatment were obtained by volumetric hydrogen chemisorption on a Micromeritics ASAP 2020 instrument. The catalyst (100 mg) was loaded in a U-shaped quartz reactor, where it was initially evacuated at 303 K for 1 h. Afterwards it was reduced in flowing H_2 at 923 K for 60 min (heating rate 10 K/min). After reduction, the samples were evacuated at 673 K for 240 min, then cooled down to 303 K, and evacuated for another 30 min. The adsorption isotherm measurements were carried out at 303 K and 191 K based on the adsorbed amount of hydrogen at different pressures in the range 2–200 mmHg. Adsorbed volumes were determined by extrapolation to zero pressure of the linear part of the adsorption isotherm in the interval 2–100 mmHg. A chemisorption stoichiometry of H:Rh = 1:1 was assumed. Gatica et al. [30,31] reported the influence of different variables like reduction and analysis temperature on the H_2 chemisorption results. They stated that the use of H_2 adsorption at 191 K was a suitable tool for the estimation of the rhodium dispersion for catalysts containing cerium because no significant spillover occurs at such low temperature.

2.3. Catalytic activity

Catalytic partial oxidation of methane was carried out in a quartz reactor (10 mm i.d.) at atmospheric pressure. A movable thermocouple was placed in a quartz tube inside the reactor, enabling the measurement of an apparent gas temperature profile. Methane was fed separately from the air feed and the two streams were mixed before entering the reactor. Water was condensed before the product was analyzed. The furnace temperature was measured between the quartz reactor and the inside of the furnace at the same axial position as the outlet of the catalyst bed. Typically, 10–100 mg of pelletized catalyst (sieve fraction 100–200 μm) diluted with α-alumina were used in each measurement. The gas hourly space velocities (GHSV) were in the range of 53–1500 $L_{CH_4}/(g_{cat}\,h)$. The reaction temperature interval was from 673 to 1173 K. A reactant mixture of methane and air was used with a ratio $CH_4:O_2:N_2$ of 2:1:3.72. The product analysis was carried out by a gas chromatograph (GC) (Agilent 6980) equipped with a thermal conductivity detector (TCD) and a flame ionization detector (FID). The H_2 and H_2O concentrations were determined through the hydrogen and oxygen balance, respectively. Results are presented as function of the outlet temperature, which is defined as the temperature at the outlet of the catalytic bed measured with an internal movable thermocouple.

The ignition–extinction behavior was studied for catalysts with a loading of 0.1 and 0.5 wt.% of Rh by increasing gradually the furnace temperature from 573 K to 1173 K at a heating rate of 10 K/min. Subsequently, the reactor was cooled down until the reaction became autothermal.

The stability of the catalysts was studied by increasing the furnace temperature to 1173 K with a heating rate of 10 K/min. The catalyst was maintained on reaction conditions during 48 h while product analysis was performed each 23 min.

3. Results and discussion

3.1. Structural properties of the mixed nanocomposites

3.1.1. XRD results

X-ray diffraction reflects the changes of the crystalline structures of the materials when they are treated at different temperatures. Fig. 1a presents the XRD patterns of the Al_2O_3 sample (dashed lines) aged at temperatures from 1173 to 1473 K for 5 h in static air. The XRD patterns showed that δ- and θ-alumina appeared when the alumina was treated at the lower temperatures, 1173 and 1273 K, respectively, although δ-Al_2O_3 was still dominating in this temperature range. However, when the sample was aged at 1373 K the α-Al_2O_3 phase was dominant in the solid. Further treatments at higher temperatures (1423 or 1473 K) led to the complete formation of α-Al_2O_3, accompanied with the particle size growth, and the closure of the pore structures. Therefore, the phase transition of Al_2O_3 was expected to happen in the operational temperature range for CPO. When γ-Al_2O_3 is employed as catalyst support, it gradually transits to its thermostable phase α-Al_2O_3.

It has been reported that the driving force for the sintering of γ-Al_2O_3 was to lower the surface energy [32]. By coating with high-temperature stable additives such as oxides on the high surface area γ-Al_2O_3, it was possible to delay the transition to α-alumina. Here, $Zr_xCe_{1-x}O_2$ was introduced into the Al_2O_3 by a simple evaporation drying procedure. The synthesis of 20 wt.% ZrO_2–Al_2O_3 and CeO_2–Al_2O_3 has been previously reported by our group [33]. An exhaustive XRD–Raman study was done with the objective of gaining knowledge on the alumina phase transformation and the behavior of the additional oxide.

Typically, $Zr_xCe_{1-x}O_2$–alumina nanocomposites were treated at temperatures between 1173 and 1473 K for 5 h. As an example, Fig. 1a displays a comparison of the XRD profiles for $Zr_{0.5}Ce_{0.5}O_2$–alumina nanocomposites (solid line) and the single alumina sample (dashed line). The addition of the second compound significantly retards the formation of α-Al_2O_3. For instance, there were no obvious peaks of α-Al_2O_3 when the composite was aged at 1373 K for 5 h. In contrast, these specific peaks for α-Al_2O_3 were dominant in the raw Al_2O_3 under the same conditions in Fig. 1a. On the other hand, when $Zr_{0.5}Ce_{0.5}O_2$–alumina was treated at 1423 K for 5 h, the appearance of weak peaks associated with the α-Al_2O_3 formation was observed and furthermore, the α-phase was dominant after calcination at 1473 K for 5 h.

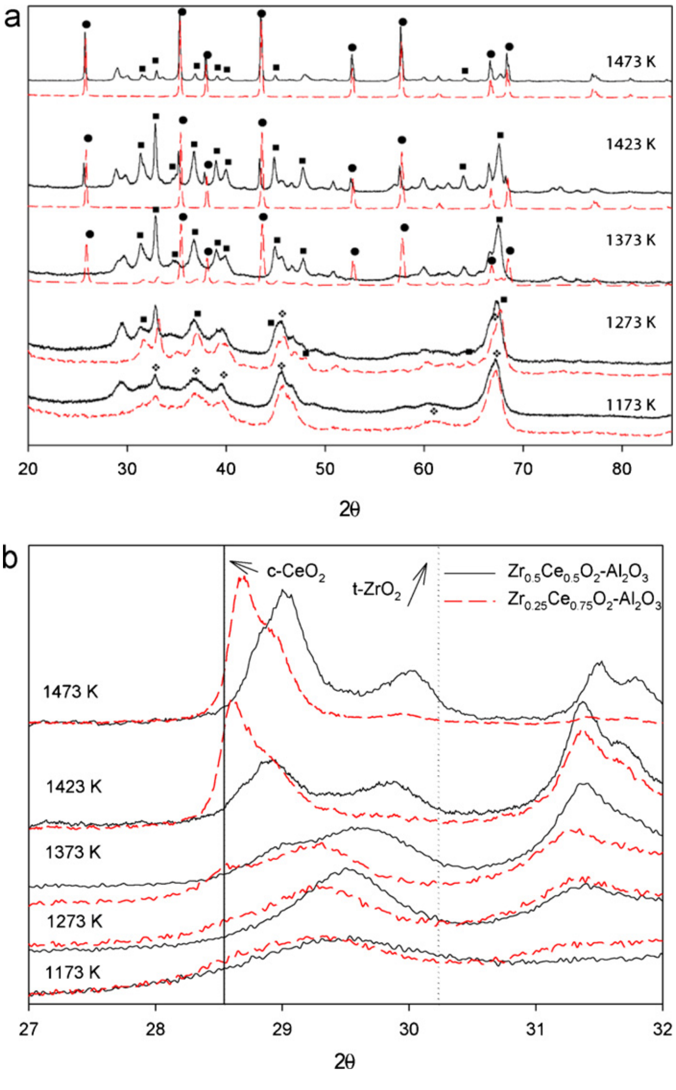

Fig. 1. (a) X-ray diffraction patterns of alumina (▬ ▬ ▬ ▬) compared with $Zr_{0.5}Ce_{0.5}O_2$–Al_2O_3 (—). Samples are calcined for 5 h at temperatures between 1173 and 1473 K. Data collected at 0.02°/step between 2θ = 20° and 85° (●, α-Al_2O_3; ■, θ-Al_2O_3; ❖ , δ-Al_2O_3). (b) X-ray diffraction patterns of $Zr_{0.25}Ce_{0.75}O_2$–Al_2O_3 (▬ ▬ ▬ ▬) compared with $Zr_{0.5}Ce_{0.5}O_2$–Al_2O_3 (—). The samples are calcined for 5 h at temperatures between 1173 and 1473 K. The vertical solid line marks the characteristic position of cubic ceria (2θ = 28.54°) and the vertical dotted line marks the tetragonal zirconia (2θ = 30.2°). Data collected at 0.0057°/step between 2θ = 27° and 32°.

The role of the citric acid in the preparation of these composite was also studied using XRD measurements. It was observed that without employing the chelating agent the contribution to the α-alumina formation is larger (data not shown here). The citric acid might help to disperse the zirconia on the alumina by improving the interaction between the alumina surface (rich in –OH groups) and the zirconia (or Ce–) containing complex. In a more extensive study of the preparation method we demonstrated that the in situ polymerization process is very crucial for the deposition of the active component on the surface of the alumina matrix [26].

In order to verify the shape and positions of the peaks, data collection with a slow scanning speed was performed

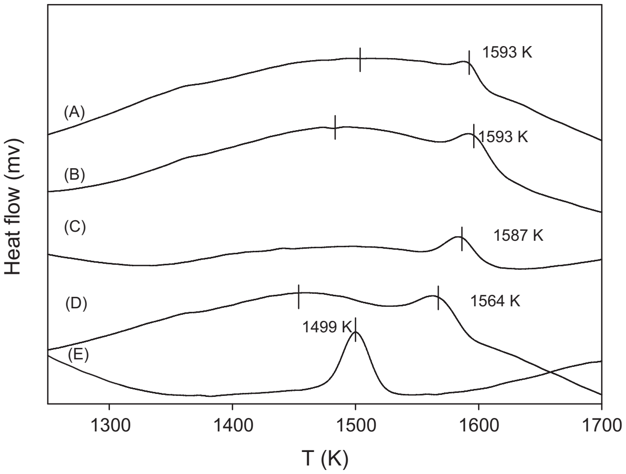

Fig. 2. DTA profiles for $Zr_xCe_{1-x}O_2$–Al_2O_3 measured in the temperature interval 1250 K and 1700 K (heating rate: 10 K/min; air flow = 80 mL/min) (A = $Zr_{0.25}Ce_{0.75}O_2$–Al_2O_3; B = $Zr_{0.5}Ce_{0.5}O_2$–Al_2O_3; C = ZrO_2–Al_2O_3; D = CeO_2–Al_2O_3; E = Al_2O_3).

for $Zr_{0.5}Ce_{0.5}O_2$–Al_2O_3 and $Zr_{0.25}Ce_{0.75}O_2$–Al_2O_3 in the range of $2\theta = 27$–$32°$, where the detected peaks were related to the cubic CeO_2 (c-CeO_2, 28.54°) and tetragonal ZrO_2 (t-ZrO_2, 30.2°), or the mixed oxides of them. A homogeneous solid solution of zirconium and cerium mixed oxide has specific peaks between 28.54° and 30.2°. The obtained results from XRD are displayed in Fig. 1b. The characteristic peaks for these $Zr_{0.5}Ce_{0.5}O_2$ and $Zr_{0.25}Ce_{0.75}O_2$ solid solutions appeared even after aging at 1273 K. At temperatures higher than 1273 K, these solid solutions started to decompose. The formation of c-CeO_2 and the other two Zr–Ce oxide solutions were observed for the $Zr_{0.25}Ce_{0.75}O_2$–Al_2O_3 sample, whereas no c-CeO_2 phase was produced on the $Zr_{0.5}Ce_{0.5}O_2$–Al_2O_3 sample. According to the phase diagram for CeO_2–ZrO_2 mixed oxides, they decompose after aging at temperatures between 1273 K and 1673 K into a tetragonal ZrO_2-rich and a cubic CeO_2-rich phases which are thermodynamically stable at such temperatures [34]. This behavior was clearly observed for both materials after aging at 1473 K. Due to the different chemical composition in these two initial mixed oxides, higher ZrO_2 fraction in the initial mixed oxide composition led to the location of the split peak closer to the tetragonal ZrO_2 phase as shown in Fig. 1b, whereas lower ZrO_2 fraction in the mixed oxide ($Zr_{0.25}Ce_{0.75}O_2$) gave a diffraction peak closer to the c-CeO_2. Besides, at these calcination temperatures, no ZrO_2 peak was detectable for those samples. This might indicate that the Zr was incorporated into the c-CeO_2 lattice even after the decomposition of the initial material.

3.1.2. DTA results

DTA provided information about the phase transition in the different materials. The results for $Zr_xCe_{1-x}O_2$–Al_2O_3 composites are presented in Fig. 2. Due to the similarity of the profiles for all the samples at temperatures less than 1273 K, only the profiles in the range 1273–1773 K are shown here. An exothermic peak at temperatures higher than 1499 K was observed for all the materials. Such a peak corresponds to the formation of α-alumina, which presents the better crystallinity among the alumina phases. The delay in the appearance of this peak may be related with a higher thermostability. For instance, peaks in the range of 1564–1593 K were observed for the composite with $Zr_xCe_{1-x}O_2$, whereas a peak at 1499 K was observed for the individual Al_2O_3 sample, indicating a difference of 60–100 K between them. Summarizing, the DTA results in Fig. 2 clearly show that the $Zr_xCe_{1-x}O_2$–Al_2O_3 through the citric acid method, can effectively retard the formation of α-alumina and produce a composite with higher thermostability.

3.1.3. Scanning electron microscopy

The morphology of the $Zr_{0.5}Ce_{0.5}O_2$–Al_2O_3 nanocomposites after heat treatment at 1173 K and 1473 K, is presented in Fig. 3a and b, respectively. SEM images of the sample aged at 1173 K showed the presence of agglomerated nanosized particles in Fig. 3a. The SEM micrograph in Fig. 3b for the sample treated at 1473 K showed the increased particle size of the material due to the formation of α-alumina. However, some small particles in the nanosize range remained on the surface, showing the benefits of employing an additional oxide in the support formulation. Fig. 3c shows the TEM micrograph for a $Zr_{0.5}Ce_{0.5}O_2$–Al_2O_3 sample calcined at 1173 K during 5 h. The ability of the alumina to highly disperse the $Zr_xCe_{1-x}O_2$ phase was clearly demonstrated by the found particle in the nanorange.

3.1.4. Raman spectroscopy study

Two lasers in the ultraviolet (UV) and visible range were employed in the Raman spectroscopy study to further identify the structural properties of the composites [35,36]. The use of these two lasers emitted at different wavelength may give surface and bulk information about the samples. UV-Raman spectroscopy was more sensitive at the surface region (the mixed oxides), whereas two operation windows were identified in visible Raman. From 1000 cm^{-1} to 2000 cm^{-1} the alumina phase transitions could be followed, and the bands related to the additional oxide were located in the interval 200–700 cm^{-1}. According to the literature, six Raman active modes ($A_{1g} + 3E_g + 2B_{1g}$) would be expected for tetragonal ZrO_2 (space group $P4_2/nmc$) [22,37], while for the cubic fluorite structure only the F_{2g} mode centred at around 460 cm^{-1} is Raman active [22,38–44]. According to the cerium content, ceria–zirconia ceramics composites exist in three different phases, namely monoclinic, tetragonal, and cubic [22,37,45,46]. Three tetragonal phases could be distinguished on the bases of XRD and Raman: t, t' and t''. The t'' phase is intermediate between t′ and cubic phase, and it shows no tetragonality of the cation sublattice.

A XRD and Raman spectroscopy study on the 20 wt.% ceria–alumina, zirconia–alumina composites derived from the same preparation method was reported elsewhere [33], demonstrating that combined UV and visible Raman spectroscopy coupled with XRD was a powerful tool for studying the structure of the nanocomposites. It was found that the presence of a coating layer of $Zr_xCe_{1-x}O_2$ on the surface of the alumina led to a higher thermostability for the prepared nanocomposites.

3.1.4.1. Alumina studied under visible Raman.

Fig. 4a and b shows the visible Raman spectra for Al_2O_3 and $Zr_{0.5}Ce_{0.5}O_2$–Al_2O_3, respectively. Samples were treated for 5 h at temperatures from 1273 to 1473 K. The peaks at 1370 and 1397 cm^{-1} are typical for the α-phase. These peaks appeared in the raw Al_2O_3 when it was aged at temperatures higher than 1273 K in Fig. 4a, whereas they appeared in $Zr_{0.5}Ce_{0.5}O_2$–Al_2O_3 when it was aged at temperatures over 1423 K in Fig. 4b. In addition, a small amount of θ-phase (1173 and 1250 cm^{-1}) was still detected in $Zr_{0.5}Ce_{0.5}O_2$–Al_2O_3 but not in the Al_2O_3 sample even after treatment at 1373 K. These results were in agreement with the observed ones by XRD in Fig. 1a where it was shown that the introduction of $Zr_{0.5}Ce_{0.5}O_2$ stabilizes the θ-alumina phase.

The alumina phase composition for samples calcined at 1373, 1423 and 1473 K is presented in Fig. 4c. The contents of the α- and θ-phases were calculated by integration of the corresponding Raman peaks for each of the phases. These results were further confirmed by the analysis performed for the XRD patterns on the bases of the Rietveld fitting [27]. It was observed that the alumina sample was

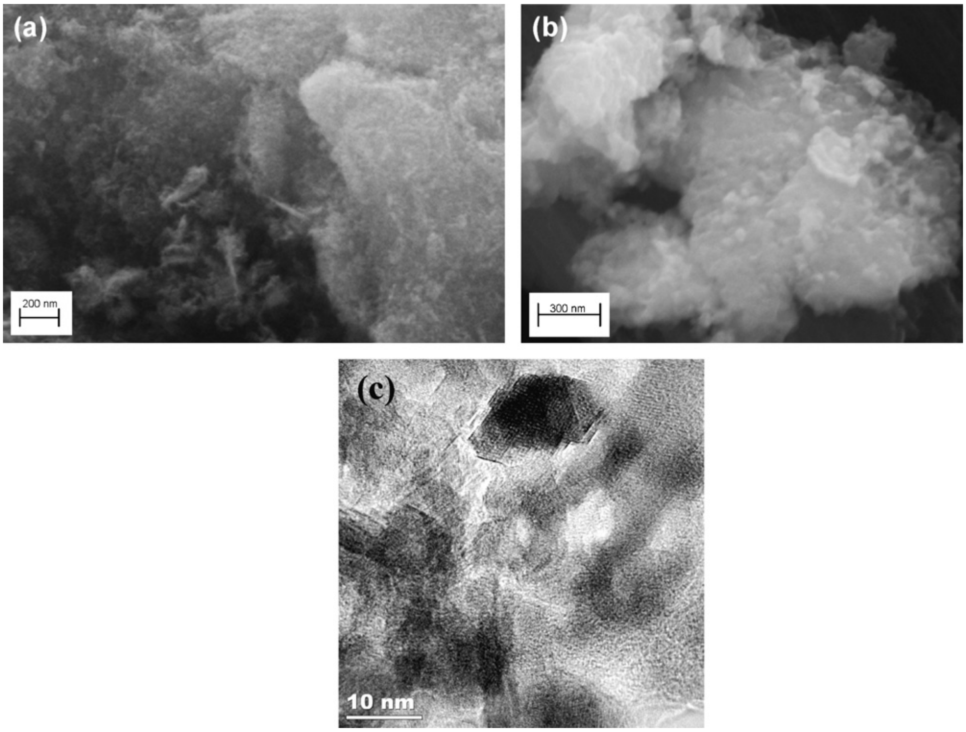

Fig. 3. SEM micrograph of $Zr_{0.5}Ce_{0.5}O_2/Al_2O_3$ calcined at (a) 1173 K and (b) 1473 K for 5 h, and (c) TEM micrograph of $Zr_{0.5}Ce_{0.5}O_2/Al_2O_3$ calcined at 1173 K for 5 h.

composed mainly by the α-phase after being aged at 1373 K for 5 h. However, the introduction of ZrO_2 or CeO_2 to form the nanocomposites provoked a delay in the alumina phase transition. Thus, just a small trace of the α-phase could be detected for the samples after calcination at 1373 K during 5 h. Additionally it was observed that the mixed oxide $Zr_xCe_{1-x}O_2$ (*i.e.* $Zr_{0.5}Ce_{0.5}O_2$ or $Zr_{0.25}Ce_{0.75}O_2$) played a more pronounced role in the stabilization of the alumina than the single oxides, *i.e.* ZrO_2 and CeO_2. Fig. 4c shows that after calcination at 1423 K, the materials with ZrO_2 and CeO_2 present around 80% of the alumina under the α-phase, whereas the mixed nanocomposites show values around 20%. This trend was further confirmed for additional samples prepared with a loading of Zr–Ce oxide of 20 wt.% (data not shown here).

3.1.4.2. Mixed oxide studied under visible Raman. Visible Raman has proved to be a useful tool for investigating the nature of the Zr–Ce oxide in the Raman shift interval 200–700 cm^{-1}, where the adsorption due to the M–O stretching is observed, thus, making it possible to follow the evolution of the additional oxide into the nanocomposite samples. For the materials studied in this contribution we did not observe any signal except in the case of the CeO_2–Al_2O_3 nanocomposite where a band at 465 cm^{-1} was found (data not shown here). This band was due to the F_{2g} Raman active mode of the cubic fluorite structure. The importance of this peak increased with the calcination temperature, even though its intensity was always low.

3.1.4.3. Mixed oxide studied under UV-Raman. Raman spectra under UV radiation were recorded for the materials treated at temperatures between 1173 K and 1473 K. Due to the low loading and low crystallinity of the $Zr_xCe_{1-x}O_2$, difficulties arise to distinguish any peak for the sample treated at low temperatures. Thus, just the spectra at 1473 are presented here. Fig. 4d shows a comparison of the UV-spectra for the ZrO_2–Al_2O_3 (A), $Zr_{0.5}Ce_{0.5}O_2$–Al_2O_3 (B) and $Zr_{0.25}Ce_{0.75}O_2$–Al_2O_3 (C) and CeO_2–Al_2O_3 (D).

A single peak at ca. 454 cm^{-1} was identified for the CeO_2–Al_2O_3 (D) nanocomposite ascribed to the F_{2g} Raman active mode of the cubic fluorite structure, while bands at 270, 315, 380, 419 and 647 cm^{-1} were observed for the ZrO_2–Al_2O_3 nanocomposite (A). The peaks at ca. 270, 315, and 647 cm^{-1} were related to the tetragonal phase (t-ZrO_2), whereas the ones at 380 and 419 cm^{-1} are typical for the monoclinic phase (m-ZrO_2). Moreover, two bands at 465 and 611 cm^{-1} were present in the case of $Zr_{0.25}Ce_{0.75}O_2$–Al_2O_3 (C). The peak at 465 cm^{-1} is consistent with the presence of a cubic $Zr_xCe_{1-x}O_2$ phase. The broadening of this peak could be related to the partial substitution in the lattice of Ce^{4+} by Zr^{4+} cations [45]. The peak at ca. 610 cm^{-1} was previously attributed to a tetragonal displacement of the oxygen atoms from the ideal tetrahedral sites, and related with the presence of the t' phase of $Zr_xCe_{1-x}O_2$ [47]. Such results might be explained by the segregation of the mixed oxides into two phases after calcination at 1473 K. One of the phases might be cubic (rich in cerium), and the other one tetragonal (rich in zirconia). This was in agreement with the results previously found by XRD experiments, and summarized in Fig. 1b. Furthermore, the sample $Zr_{0.5}Ce_{0.5}O_2$–Al_2O_3 (B) presents a band around 631 cm^{-1}, a small band at around 460 cm^{-1} is also observed, but relatively hidden by the higher intensity of the peak at 631 cm^{-1}. This might be related with the increased importance of the tetragonal phase compared with the cubic $Zr_xCe_{1-x}O_2$, due to the higher zirconium loading in the sample.

Since UV-Raman is surface sensitive for those materials which absorb UV-light [35,36] (such as zirconia), this confirms the existence of a mixture of t-ZrO_2 and m-ZrO_2 on the surface of the alumina after treatment at 1473 K during 5 h. It seems that the monoclinic phase appears at the surface at 1473 K, since no obvious XRD peaks related to such phase were observed under these conditions (data not shown here) for the ZrO_2–Al_2O_3 nanocomposite. Furthermore it was confirmed the formation of a coating layer of $Zr_xCe_{1-x}O_2$ on the surface of the alumina.

3.2. Textual properties of the mixed nanocomposites

Fig. 5 gives the BET surface area evolution of alumina and alumina based nanocomposites after heat treatment at 1173, 1273,

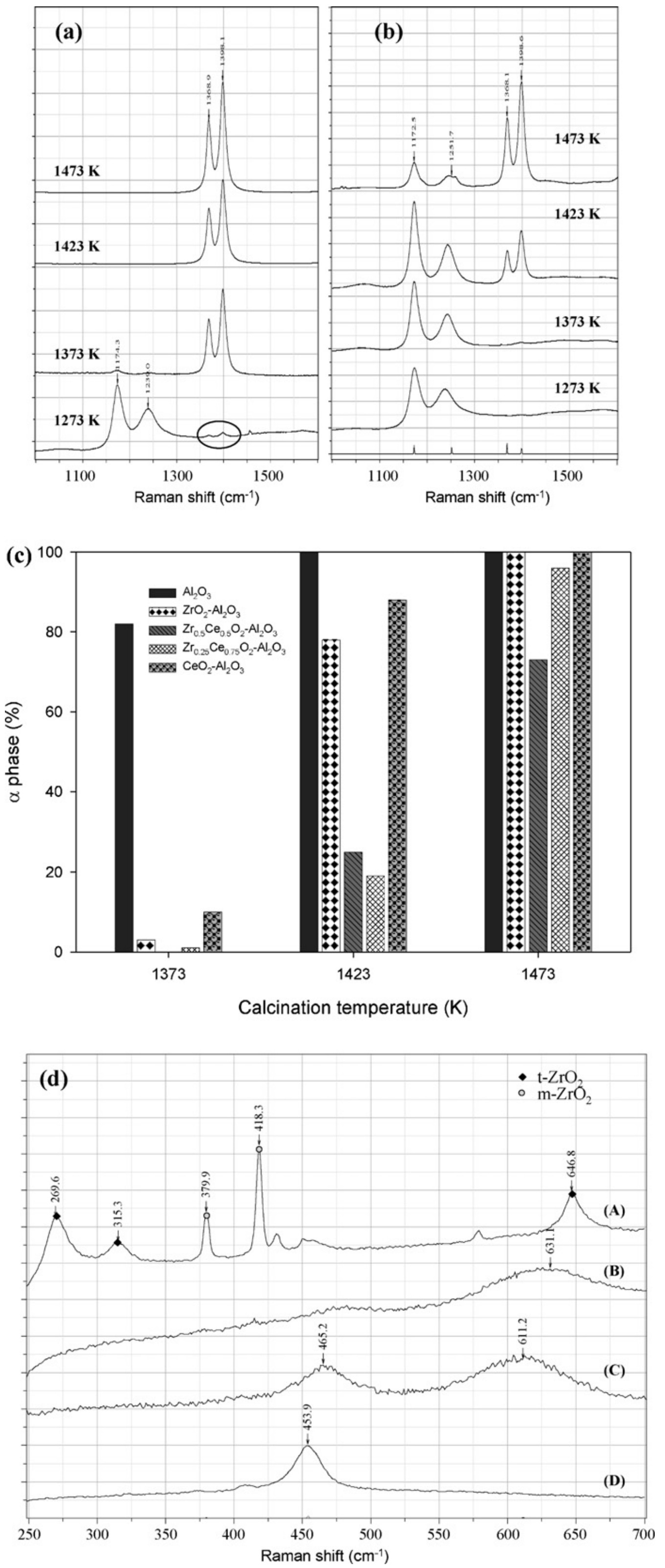

Fig. 4. (a and b) Visible Raman spectra of (a) Al_2O_3 and (b) $Zr_{0.5}Ce_{0.5}O_2–Al_2O_3$. Samples are calcined at temperatures between 1273 and 1473 K for 5 h. Spectra recorded at 632 nm in the Raman shift interval between 1000 and 2000 cm^{-1}. (c) Summary of the alumina phases composition for samples treated at 1373, 1423 and 1473 K. Heat treatments during 5 h are used. The phase composition is calculated in bases of XRD and Raman. Raman results are obtained by integration of the peaks related to each of the phases. (d) UV Raman spectra of (A) $ZrO_2–Al_2O_3$; (B) $Zr_{0.5}Ce_{0.5}O_2–Al_2O_3$; (C) $Zr_{0.25}Ce_{0.75}O_2–Al_2O_3$; (D) $CeO_2–Al_2O_3$. Samples are aged at 1473 K for 5 h. Spectrum recorded at 325 nm in the Raman shift interval between 250 and 700 cm^{-1} (◆, t-ZrO_2; ○, m-ZrO_2).

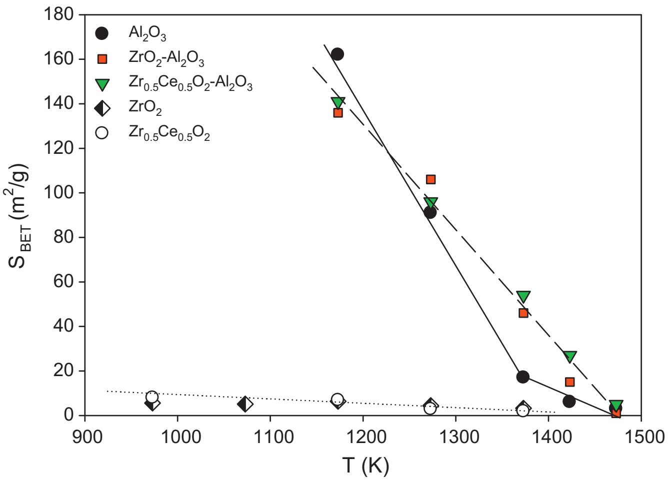

Fig. 5. BET surface area evolution with the aging temperature for $Zr_xCe_{1-x}O_2–Al_2O_3$ nanocomposites prepared with citric acid.

1373, 1423 and 1473 K for 5 h. In addition, the surface area evolution for the individual ZrO_2 and $Zr_{0.5}Ce_{0.5}O_2$ is presented. Those materials were prepared by the Pechini method and a much lower surface area was observed (less than 5 m^2/g). The low surface area of ZrO_2 or $Zr_{0.5}Ce_{0.5}O_2$ at high temperature might be related to the particle growth.

Due to the relatively low loading of $Zr_xCe_{1-x}O_2$, the surface area of the composites was close to Al_2O_3 when the samples were treated at temperatures lower than 1273 K. Increasing the aging temperature further to 1373 K, the surface area of the composites was higher compared with the Al_2O_3 samples. The heat treatment at 1473 K led to a very low surface area both for the composite and the Al_2O_3. A linear relationship between the surface area of the $Zr_{0.5}Ce_{0.5}O_2–Al_2O_3$ composites and the calcination temperature between 1273 and 1473 K was found. Another relationship between the surface area and the individual Al_2O_3 was also presented in Fig. 5. With the increased calcination temperature, sintering of the materials was happening. When the α-alumina started to be present in the nanocomposites, the surface area dropped dramatically and the crystal size of the alumina increased drastically. It was found a faster decrease of surface area for the Al_2O_3 than for the composites, implying that the Al_2O_3 was more sensitive to the calcination temperature. This observation, consistent with the XRD and DTA and Raman spectroscopy results, clearly exhibited a synergism stabilization mechanism between Al_2O_3 and $Zr_xCe_{1-x}O_2$, the phase transformation of the alumina was delayed due to the presence of the Zr–Ce oxide, whereas the sintering of c-CeO_2 or the phase transformation of t-ZrO_2 to m-ZrO_2 were also postponed due to the alumina.

3.3. Hydrogen chemisorption

Different Rh loadings, namely, 0.1 and 0.5 wt.% were used here. Prior to the chemisorption measurements, the Rh supported on the composite samples were aged at 1173 K for 5 h. The particle sizes for the Rh nanoparticles over the different supports are shown in Table 1. Those results are based on the H_2-chemisorption performed at 303 or 191 K. The calculated particle size belonged to the range 2.7–4.2 nm. Catalysts with a Rh loading of 0.1 wt.% had slightly higher dispersion and smaller particle size than those with a loading of 0.5 wt.%. Besides, slightly higher dispersions were obtained for those catalysts containing Ce, being the dispersions similar on CeO_2, $Zr_{0.5}Ce_{0.5}O_2$ and $Zr_{0.25}Ce_{0.75}O_2$ based nanocomposites.

Table 1
Rh dispersion (%) and particle size (nm) values calculated in bases of H_2 chemisorption results. Irreversible H_2 adsorption at 303 K and 195 K calculated assuming Langmurian adsorption.

	Rh loading 0.1 wt.%		Rh loading 0.5 wt.%	
	Dispersion (%)	Particle size (nm)	Dispersion (%)	Particle size (nm)
Al_2O_3[a]	29	3.8	26	4.2
ZrO_2–Al_2O_3[a]	33	3.3	26	4.2
$Zr_{0.5}Ce_{0.5}O_2$–Al_2O_3[b]	41	2.7	30	3.7
$Zr_{0.25}Ce_{0.75}O_2$–Al_2O_3[b]	38	2.9	31	3.6
CeO_2–Al_2O_3[b]	41	2.7	28	3.9

[a] Measurements performed at 303 K.
[b] Measurements performed at 195 K.

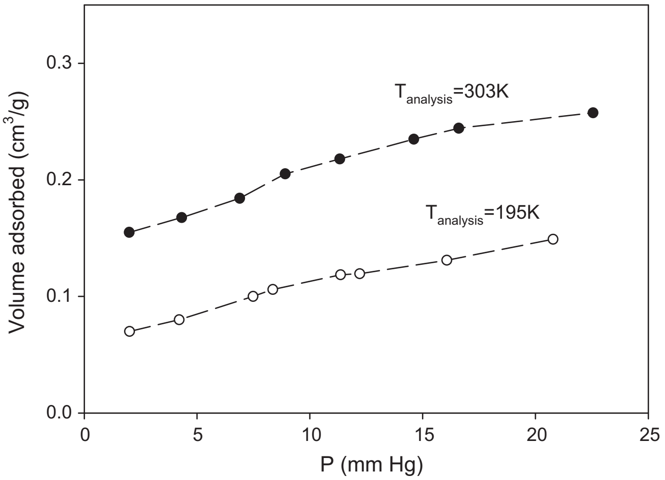

Fig. 6. Hydrogen adsorption isotherms obtained at (●) 303 and (○) 195 K for a 0.5 wt.% Rh/$Zr_{0.5}Ce_{0.5}O_2$–Al_2O_3 catalyst.

The presence of H_2 spillover is of significant concern when measuring the H_2-chemisorption in cerium containing catalyst due to an extensive adsorption of H_2 on the CeO_2 itself [21,22]. It has been reported [31,48] that an independent criterion for discriminating the presence of spillover is the time to reach the equilibrium. For all the catalysts measured in this paper, the H_2 adsorption on the metal was equilibrated within approximately 28 min at an equilibrium pressure of 2 mmHg. Those equilibration times were observed independently of the cerium content of the support, suggesting the absence of spillover. The H_2 adsorption isotherms for 0.5 wt.% Rh supported on $Zr_{0.5}Ce_{0.5}O_2$–Al_2O_3 measured at 303 and 195 K are shown in Fig. 6. Higher amounts of H_2 were adsorbed at 303 in comparison with 195 K. This behavior is related to the occurrence of spillover of hydrogen species onto the support when the measurements were performed at 303 K.

3.4. Catalytic partial oxidation of methane

3.4.1. The effect of gas flow on the catalytic performance of CPO

Axial temperature profiles of the catalyst bed were measured by a movable thermocouple placed in an internal quartz tube located inside of the reactor. Fig. 7 presents the profiles of the temperature difference ($\Delta T = T - T_{oven}$) in the catalyst bed and oven along the reactor at three different gas hourly space velocities (GHSVs) during the CPO reaction over a 0.5 wt.% Rh/ZrO_2–Al_2O_3 catalyst. The temperature difference assigned to the quartz tube was neglected. In all of these different GHSVs, an increase of ΔT was observed at the reactor inlet zone, followed by a decrease of ΔT at the reactor outlet zone, giving a peak of maximum ΔT (>0), implying the formation of hot spots. At a fixed GHSV, this maximum ΔT decreased when the oven temperature was increased. In addition, this maximum ΔT value was also strongly dependent on the GHSV. For example, when the furnace temperature was 973 K, the value of the maximum ΔT was 35, 80 and 130 K for GHSV equal to 53, 169 and 1500 L_{CH_4}/(g h), respectively. Lower GHSV gave a lower maximum ΔT at the same oven temperature. Furthermore, obviously negative ΔT (<0) was observed for the highest oven temperatures and lowest GHSV (*i.e.* 53 L_{CH_4}/(g h)). This negative ΔT gradually disappeared as the GHSV increased. Thus, in the case of GHSV = 1500 L_{CH_4}/(g h), it did not appear.

Different GHSV can give mass and heat transfer information for the CPO process. It is generally accepted that there are two different reaction zones in the CPO process: oxidation zone close to reactor inlet, followed by a reforming zone [6,49]. In the oxidation zone, the strongly exothermic reactions characterized by the fast consumption of oxygen, are dominating, while in the reforming zone, consumption of CH_4 via endothermic reactions occurs. The oxidation reaction rate is 2 orders of magnitude higher than for the reforming reaction [50,51]. Due to the very fast reaction rate in the oxidation zone, after the ignition, the oxidation reaction is controlled by the diffusion rate of oxygen [9,52]. More heat released occurs due to a faster diffusion rate of oxygen at a high space velocity, thus giving a higher temperature difference, as indicated by the different values of ΔT confirmed in Fig. 7.

The reforming reaction rate increased at higher temperatures, thus more heat was needed to proceed. Therefore, the heat released by the oxidation reaction could be offset by the following reforming. Under the condition of lower GHSV = 53 L_{CH_4}/(g h), due to less heat released by the oxidation reaction, this heat could be effectively offset by the reforming reaction, thus giving a lower ΔT for higher oven temperatures and further indicated by the appearance of the negative ΔT. However, increasing the GHSV to 1500 L_{CH_4}/(g h), the heat released by the oxidation reaction exceeded the heat required for the reforming reaction, showing a positive ΔT in the entire catalyst bed.

The above results, pointed out in Fig. 7a–c, showed that higher GHSV led to more heat released and a higher ΔT in the catalyst bed. Therefore, GHSV to 1500 L_{CH_4}/(g h) was used in the present study to investigate the effect of the loading of Rh, the composition of the support, the reaction temperature and GHSV on the activity, selectivity, and stability in the CPO process.

Fig. 7d shows the results of the catalytic testing for several GHSVs for the 0.5 wt.% Rh/$Zr_{0.5}Ce_{0.5}O_2$–Al_2O_3 catalyst for an oven temperature of 873 K. The outlet gas temperature was measured with movable thermocouple placed inside of the reactor. A difference of 160 K between the lower and higher values of GHSV tested is reported in the same figure. In addition, the approach to the water gas shift equilibrium is also presented ($\eta_{wgs,eq} = (K_{EXP}/K_{EQ})_{WGS}$). It was observed that an increase in the space velocity determines an increase in methane conversion and outlet gas temperature (K). By increasing the GHSV, an increase of the heat release by the reaction occurs due to the rise in methane conversion and reactant flow rate as observed in the temperature profile in Fig. 7b–d. The approach to

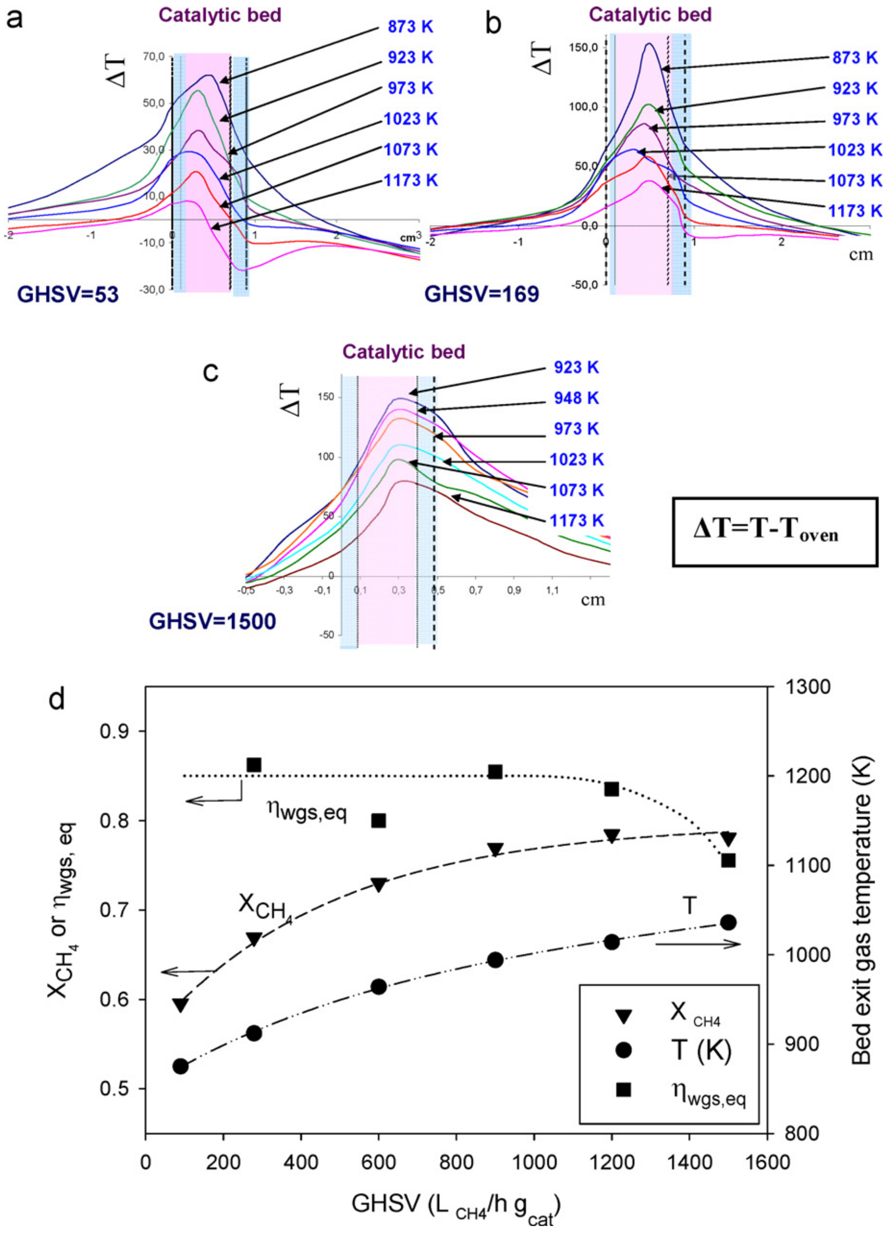

Fig. 7. (a–c) Typical axial temperature profile as function of oven temperatures between 873 and 1173 K for different GHSV ((a) GHSV = 53 L_{CH_4}/(h g_{cat}), (b) GHSV = 169 L_{CH_4}/(h g_{cat}) and (c) GHSV = 1500 L_{CH_4}/(h g_{cat})). Catalyst 0.5 wt.% Rh/ZrO_2–Al_2O_3. (d) Effect of the GHSV on the CH_4 conversion and the bed gas exit temperature in the catalyst bed as a function of the approach to the WGS equilibrium. ▼, CH_4 conversion; ■, $\eta_{wgs,eq}$; ●, bed exit gas temperature (K). Furnace temperature = 873 K. Catalyst = 0.5 wt.% Rh/$Zr_{0.5}Ce_{0.5}O_2$–Al_2O_3.

equilibrium of the water gas shift reaction (WGS) was close to one at relatively low GHSVs, indicating that WGS was in equilibrium, and the distribution of H_2, CO, CO_2 and H_2O were determined by the equilibrium instead of kinetics at these conditions. However, when the GHSV was increased, the value of the approach to the WGS equilibrium was decreasing suggesting that the gas distribution could be affected by the kinetics.

3.4.2. The effect of support composition on the ignition behavior in the CPO process

Catalytic testing of 0.5 wt.% and 0.1 wt.% Rh loading was performed. Thus, Fig. 8 shows the results in terms of methane conversion as well as the selectivity to H_2, CO and CO_2 for the CPO process for the catalysts with 0.1 wt.% Rh loading. Values of conversion and selectivity for the thermodynamic equilibrium (dashed line) are also reported in the same figures for the sake of comparison.

Previous studies under working conditions showed that the ignition–extinction behavior of Rh based catalyst for CPO is directly related with the oxidation state of the Rh [6,53,54]. The consumption of methane and oxygen started below the ignition temperature where the total oxidation of methane to H_2O and CO_2 occurred when the Rh was in the oxidized state. After a certain time and temperature an intermediate oxidation state of the Rh was happening [55]. The reaction ignited at the same time as the Rh was reduced and the extinction happened when the Rh was re-oxidized [54].

As shown in Table 2 the light-off temperature for methane conversion was dependent on the metal loading: the light-off temperature was in the range of 945–995 K for the 0.5 wt.% Rh based catalyst and 1040–1140 K for the 0.1 wt.% Rh based catalysts.

Table 2
Variation of the ignition temperature for CPO as a function of the employed support and the Rh loading.

	Ignition temperature (K)	
	0.5 wt.% Rh	0.1 wt.% Rh
CeO_2–Al_2O_3	945	1037
$Zr_{0.25}Ce_{0.75}O_2$–Al_2O_3	970	
$Zr_{0.5}Ce_{0.5}O_2$–Al_2O_3	988	1073
ZrO_2–Al_2O_3	993	1113

The observed trend clearly indicates the benefits of using cerium oxide in the formulation of the catalyst with the lowest ignition temperatures for the highest cerium content. Additionally, those materials containing cerium oxide presented lower ignition temperatures than those supported on ZrO_2–Al_2O_3. It has been widely reported that the introduction of small amounts of zirconium into the CeO_2 lattice promotes the oxygen mobility [56]. This behavior was attributed to the participation of bulk oxygen in the storage process.

3.4.3. *The effect of support composition and Rh loading on the catalytic performance in the CPO process*

Catalytic testing of 0.5 wt.% Rh catalysts led to similar methane conversions for all the catalysts containing cerium (around 88% for an outlet gas temperature of 1100 K), whereas a slightly lower value was observed for the ZrO_2–Al_2O_3 catalyst (around 81% for an outlet gas temperature of 1100 K). A similar situation was found on the catalyst with 0.1 wt.% Rh as shown in Fig. 8a. The trend for the conversion of methane was Rh/$Zr_{0.5}Ce_{0.5}O_2$–Al_2O_3 ≈ Rh/CeO_2–Al_2O_3 > Rh/ZrO_2–Al_2O_3 > Rh/Al_2O_3. A significantly lower conversion of methane was observed for the catalyst with 0.1 wt.% compared to the case with 0.5 wt.% Rh.

Additionally, the selectivity to CO_2, CO and H_2 were calculated for catalysts with a Rh loading of 0.1% and presented

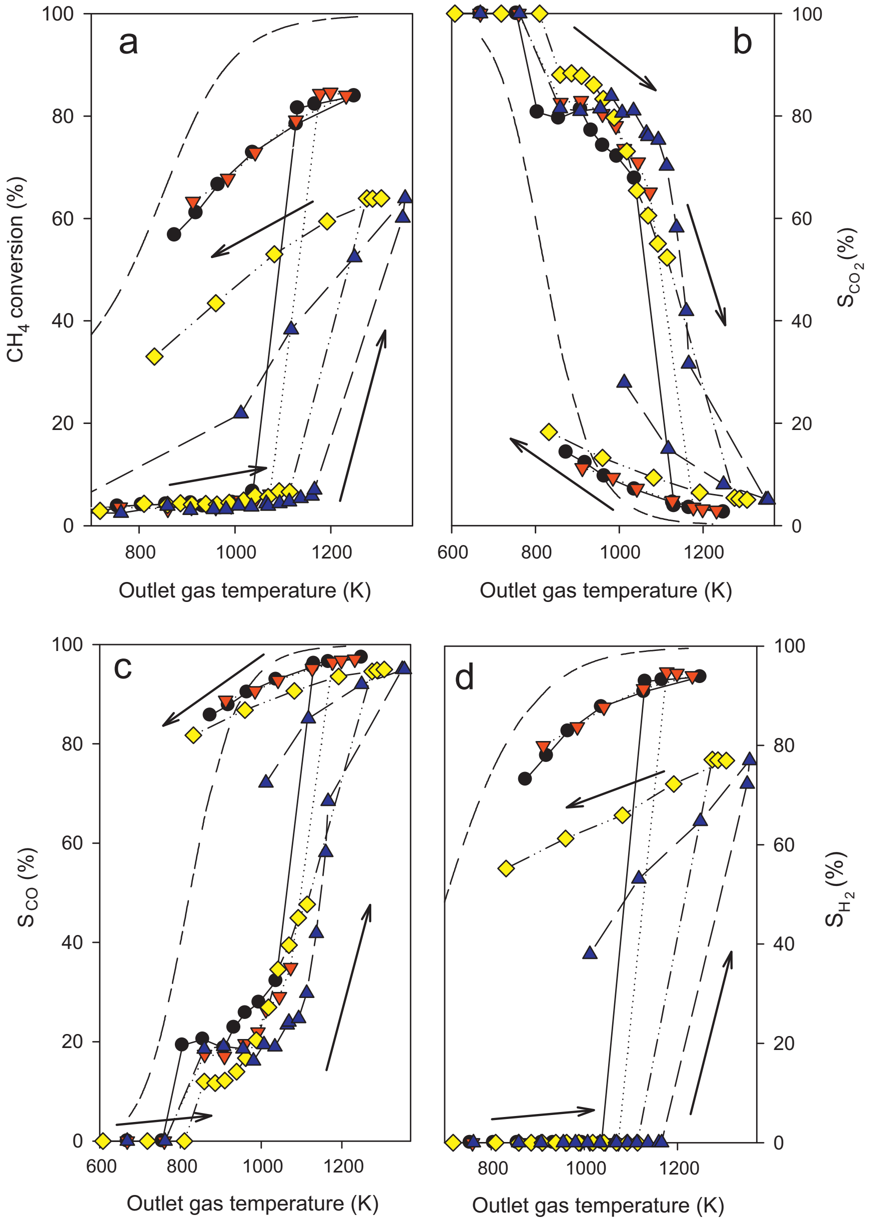

Fig. 8. (a–d) Comparison of the (a) methane conversion, (b) CO_2 selectivity, (c) CO selectivity and (d) H_2 selectivity for catalysts with a Rh loading of 0.1 (▼, Rh/$Zr_{0.5}Ce_{0.5}O_2$–Al_2O_3; ▲, Rh/Al_2O_3; ♦, Rh/ZrO_2–Al_2O_3; ●, Rh/CeO_2–Al_2O_3; - - -, equilibrium) (P = 1 atm; GHSV = 1500 $L_{CH_4}/(h\ g_{cat})$; CH_4/O_2 = 2; outlet gas temperature interval = 573–1300 K; furnace temperature interval = 573–1173 K).

Table 3
H_2/CO and approach to WGS re-equilibrium for an outlet gas temperature of 1100 K and catalyst with a Rh loading of 0.1 wt.% (P = 1 atm. GHSV = 1500 L CH_4/h g_{cat}, CH_4/O_2 = 2).

	H_2/CO	$(K_{EXP}/K_{EQ})_{WGS}$
Rh/Al_2O_3	1.2	0.2
$Rh/CeO_2–Al_2O_3$	1.9	0.6
$Rh/Zr_{0.5}Ce_{0.5}O_2–Al_2O_3$	1.9	0.7
$Rh/ZrO_2–Al_2O_3$	1.5	0.2

in Fig. 8b, c and d. The same arrangement of the H_2 and CO selectivity as for the conversion was found over these catalysts: $Rh/Zr_{0.5}Ce_{0.5}O_2–Al_2O_3 \approx Rh/CeO_2–Al_2O_3 > Rh/ZrO_2–Al_2O_3$. Higher methane conversion gave a higher selectivity to CO and H_2, and lower selectivity to CO_2.

The strong exothermicity of the methane combustion led to the formation of hot spots mainly in the catalyst entrance zone, as shown in Fig. 7c. The reliable estimation of kinetic parameters needs to be done at those conditions where the system is not transport limited. Obviously, the experiments performed here were far away from that situation, but it was still possible to make calculations to provide a comparison between experiments that were run under the same conditions. The apparent forward reaction rate ($r_{f,app}$) was calculated assuming that catalytic partial oxidation of methane was a first order reaction in methane and zero order on oxygen [57].

The global equilibrium for CPO, considering a stoichiometric initial mixture, was represented by Eq. (1):

$$CH_4 + 0.5O_2 = (1-a)CO + aCO_2 + bH_2 + (2-b)H_2O \qquad (1)$$

Coupling the reaction rate definition with the design equation for a fixed-bed reactor and considering the volume variation between products and reactants [58], Eq. (2) was obtained:

$$r_0 = F_{CH_4,0}\frac{dX_{CH_4}}{dW}\frac{1+\varepsilon \cdot X_{CH_4}}{1-X_{CH_4}} \qquad (2)$$

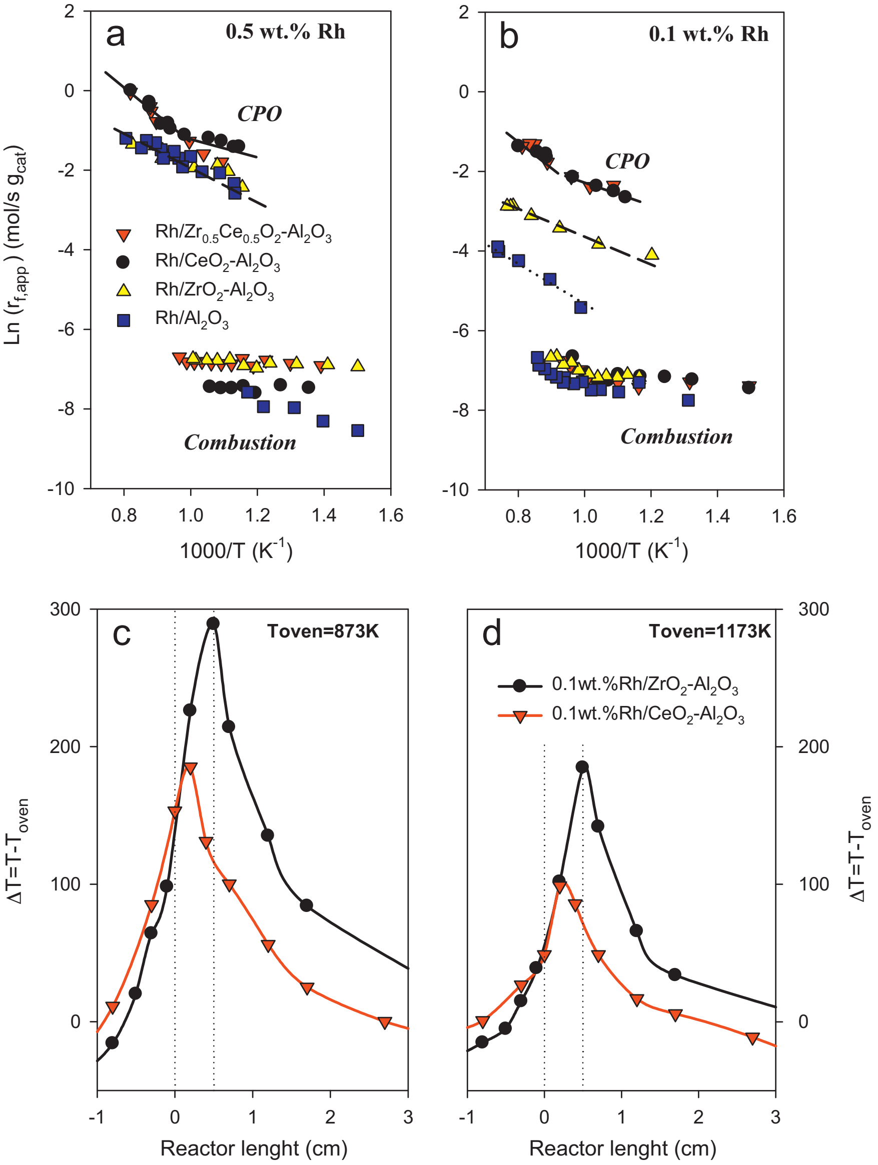

Fig. 9. (a and b) Evolution of the apparent forward reaction rate with the outlet gas temperature for catalysts with (a) Rh loading of 0.5% and (b) Rh loading of 0.1% (▼, $Rh/Zr_{0.5}Ce_{0.5}O_2–Al_2O_3$; ●, $Rh/CeO_2–Al_2O_3$; ▲, $Rh/ZrO_2–Al_2O_3$; ■, Rh/Al_2O_3) (P = 1 atm; GHSV = 1500 $L_{CH_4}/(h\ g_{cat})$; CH_4/O_2 = 2; outlet gas temperature interval = 573–1300 K; furnace temperature interval = 573–1173 K). (c and d) Axial temperature profile for an oven temperature of (c) 873 K or (d) 1773 K: ●, 0.1 wt.% $Rh/ZrO_2–Al_2O_3$; ▼, $Rh/CeO_2–Al_2O_3$ (experimental conditions: P = 1 atm; GHSV = 1500 $L_{CH_4}/(h\ g_{cat})$).

where $\varepsilon = \delta \cdot y_{0,\mathrm{CH_4}}$ being $y_{0,\mathrm{CH_4}}$ the initial mol fraction of methane and $\delta = n_{\mathrm{out}} - n_{\mathrm{in}} = 1.5$.

Additionally the approach to equilibrium (η) should be also considered [59]

$$r_{\mathrm{forward}} = \frac{r_0}{1-\eta} \quad \text{where} \quad \eta = \frac{X_{\mathrm{CH_4}}}{X_{\mathrm{CH_4,eq}}}.$$

Solving the equations above the apparent forward reaction rate was estimated with Eq. (3).

$$r_{f,\mathrm{app}} = \frac{-(1+\varepsilon)\ln(1-X_{\mathrm{CH_4}}) - \varepsilon \cdot X_{\mathrm{CH_4}}}{(1-\eta)\cdot(W/F_{\mathrm{CH_4},0})} \tag{3}$$

Fig. 9a and b is presenting the evolution of the calculated apparent forward reaction rate with the outlet gas temperature for the CPO experiments. For the tests presented here, the reaction temperature was gradually increased until the activation of the catalyst. Afterwards, the reaction temperature was gradually decreased until the reaction becomes autothermal. The pattern for methane combustion is well known. As the temperature is increased, the oxidation is initiated. A further increase in temperature leads to an exponential increase in the rate to the point where the heat generated by combustion is much greater than the heat supplied [60].

During the first period, before ignition, the conversion was under 10% and the products of the reaction were CO_2 and H_2O. Thus, only complete oxidation was taking place. After ignition, CO and H_2 were also produced. A substantial increase in the apparent forward reaction rate was observed in Fig. 9a and b after the activation indicating a pronounced difference in the apparent activation energy from the combustion to the partial oxidation zones. Besides, after activation the apparent reaction rate was gradually increasing with the temperature, probably due to the increased rate of the reforming.

Additionally, there was a short temperature interval, where the CPO was still not active but small quantities of CO were detected as shown in Fig. 8c but formation of H_2 was not observed in Fig. 8d. During this period, before ignition, some ethane and a trace amounts of ethene were also detected in the produced gas due to the gas-phase chemistry [61]. In general, the formation of C_2 hydrocarbons only occurs at temperatures above 873 K, with highest selectivity to C_2H_6 and low methane conversions. At higher conversions the selectivity to C_2 products decreased, while the yields to CO and CO_2 increase [61]. Effectively, the formation of small amounts of CO was observed from around 800 K, and coupled with the formation of C_2 products at around 1023 K. Thus, after ignition the conversion of methane increased drastically, and the selectivity towards C_2 products dropped, while it increased to CO and H_2.

After ignition the estimated apparent forward reaction rates in Fig. 9a and b presented a clear trend with higher rates for the catalysts containing Ce followed by the one containing ZrO_2 and finally the Rh/Al_2O_3 catalyst. The same trend was observed for both loadings, but the differences between the catalysts were larger when less Rh was employed. Previously it has been reported that the major benefit of employing a ceria support compared with zirconia or alumina was to achieve an improved metal dispersion, *i.e.* smaller metal particles. Slightly higher dispersions for Ce-containing catalysts were obtained as reported in Table 1. Moreover, it would be interesting to perform the catalytic testing for these materials in such conditions where the transport limitations are not important, thus, low conversions and isothermal conditions would be needed to provide a clear and more reliable analysis of the system and catalysts. Then it would be possible to estimate the existence or not of a promotional effect of Ce towards the Rh catalytic performance in CPO, additional to the slightly enhanced dispersion.

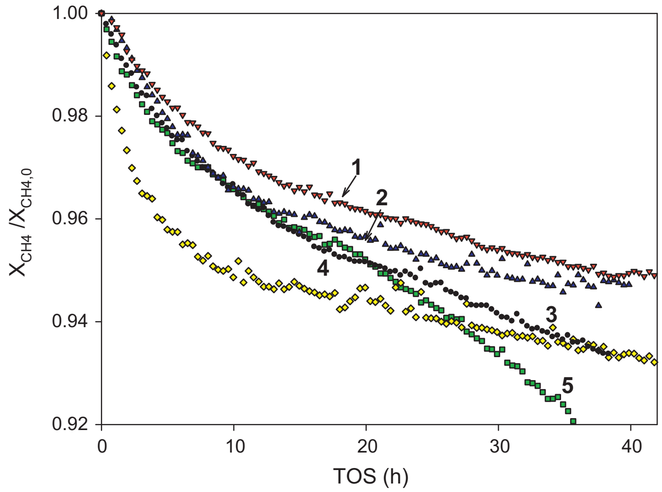

Fig. 10. (a) Comparison ratio between the CH_4 conversion and the initial CH_4 conversion during 42 h reaction for Puralox catalysts (▼, $Rh/Zr_{0.5}Ce_{0.5}O_2–Al_2O_3$ (1); ▲, $Rh/ZrO_2–Al_2O_3$ (2); ●, $Rh/CeO_2–Al_2O_3$ (3); ♦, Rh/Al_2O_3 (4); ■, $Rh/Zr_{0.25}Ce_{0.75}O_2–Al_2O_3$ (5)) (Rh loading = 0.5 wt.%; P = 1 atm; GHSV = 1500 $L_{CH_4}/(h\ g_{cat})$; T_{max} = 1230 K; $T_{furnace}$ = 1173 K; CH_4/O_2 = 2).

Furthermore, a comparison of the temperature profiles between the 0.1 wt.% $Rh/ZrO_2–Al_2O_3$ and 0.1 wt.% $Rh/CeO_2–Al_2O_3$ catalysts for oven temperatures at 873 K and 1173 K is presented in Fig. 9c and d, respectively. The greater importance of the combustion for the supported $ZrO_2–Al_2O_3$ catalyst was clearly observed, with a maximum relative temperature peak over 100 K (T_{oven} = 873 K) and around 90 K (T_{oven} = 1173 K) when compared with the $CeO_2–Al_2O_3$ and in agreement with results reported in the literature [55]. Additionally the capability of the $Rh/CeO_2–Al_2O_3$ catalyst for promoting the steam reforming reaction should be also considered [59]. Moreover, the reaction front was moved towards the outlet of the catalytic bed for the $Rh/ZrO_2–Al_2O_3$ catalyst, this would imply a delayed oxidation in the catalytic bed and a reduced length of catalyst available for the steam reforming to proceed.

3.4.4. The effect of support composition on the water-gas shift reaction and the H_2/CO ratio in the CPO process

One of the reactions included in the mechanism for the catalytic partial oxidation of methane is the water-gas shift (WGS):

$$CO + H_2O \rightarrow CO_2 + H_2 \quad \Delta H = -41\ \mathrm{kJ/mol}$$

The approach to the water-gas shift equilibrium [$\eta_{WGS} = (K_{EXP}/K_{EQ})_{WGS}$] values for an outlet gas temperature of 1100 K were calculated based on the equation below [8] and listed in Table 3.

$$\eta_{\mathrm{WGS}} = \left(\frac{K_{\mathrm{EXP}}}{K_{\mathrm{EQ}}}\right)_{\mathrm{WGS}} = \frac{P_{\mathrm{H_2}}P_{\mathrm{CO_2}}}{P_{\mathrm{H_2O}}P_{\mathrm{CO}}} \cdot \frac{1}{K_{\mathrm{EQ,WGS}}}$$

where $K_{\mathrm{EQ,WGS}}$ is the equilibrium constant for the water-gas shift reaction calculated with the outlet temperature, and P_i are the partial pressures of the different species involved. The promotional effect of ceria towards WGS reaction was clear. Thus, the approach to the WGS equilibrium represented by the ratio K_{EXP}/K_{EQ} was clearly higher for the Ce-containing catalysts (between 0.4 and 0.7) than for $Rh/ZrO_2–Al_2O_3 \approx Rh/Al_2O_3$ (around 0.2).

The H_2/CO ratio at the outlet of the reactor over 0.1 wt.% Rh catalysts for a outlet gas temperature of 1100 K is displayed in Table 3. The H_2/CO ratio was close to the equilibrium or theoretical value, 2, over 0.5 wt.% Rh catalyst containing Ce for the selected temperature. The difference in the H_2/CO ratio was more obvious on the 0.1 wt.% Rh catalysts with the following arrangement:

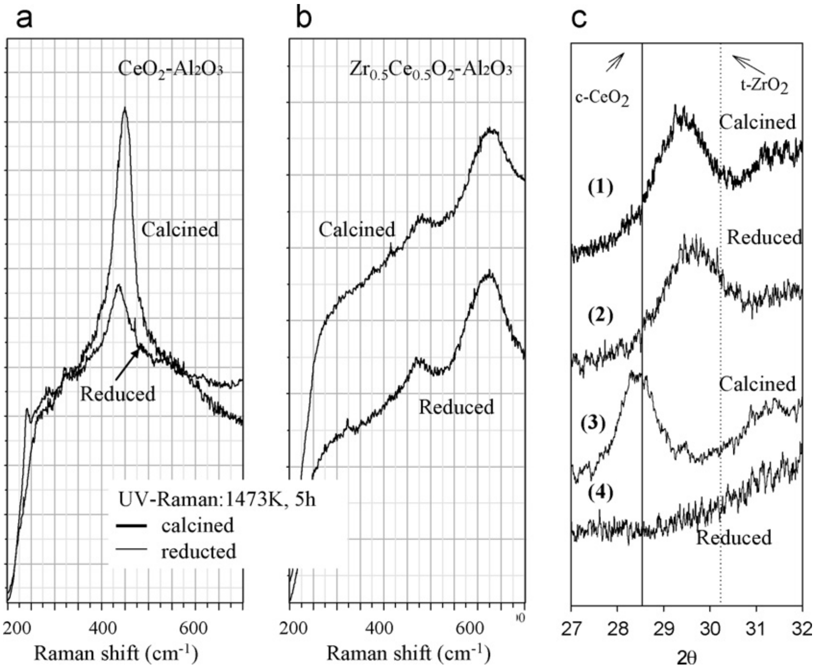

Fig. 11. (a–c) UV-Raman spectra for (a) CeO_2–Al_2O_3 and (b) $Zr_{0.5}Ce_{0.5}O_2$–Al_2O_3 nanocompoites after calcination at 1473 K during 5 h (fresh) compared with calcined samples after reduction at 1173 K in H_2 flow during 1 h (reducted). Spectrum recorded at 325 nm. (c) XRD patters of (1) fresh $Zr_{0.5}Ce_{0.5}O_2$–Al_2O_3, (2) reduced $Zr_{0.5}Ce_{0.5}O_2$–Al_2O_3, (3) fresh CeO_2–Al_2O_3 and (4) reducted CeO_2–Al_2O_3 (Fresh samples have been calcined at 1173 K for 5 h. Reduced samples are the fresh ones after reduction in H_2 flow at 1173 K during 1 h).

$Rh/Zr_{0.5}Ce_{0.5}O_2$–$Al_2O_3 \approx Rh/CeO_2$–$Al_2O_3 > Rh/ZrO_2$–$Al_2O_3 > Rh/Al_2O_3$. It was observed that with this arrangement the dispersion of Rh was the same as shown in Table 1.

3.4.5. The effect of support composition and Rh loading on the stability in the CPO process

Stability is one of the key factors in CPO due to the very high reaction temperature. Under high temperature conditions, the difference in the thermal stability of the catalytic system could be investigated. In this study, an oven temperature of 1173 K was selected to test the stability of the catalyst systems.

Fig. 10 displays a comparison of the deactivation rate for catalysts with a loading of 0.5 wt.% Rh. The deactivation rate was calculated as the ratio between the conversion at time "*t*" and the initial conversion. Catalysts were tested during 42 h. It was noticed that almost complete oxygen conversion was achieved at the outlet of the reactor.

Catalysts in Fig. 10 presented a continuous deactivation during the 48 h. Among them, the most stable performance was achieved for the catalyst supported on $Zr_{0.5}Ce_{0.5}O_2$–Al_2O_3. Additionally, Rh supported on ZrO_2–Al_2O_3 showed similar deactivation rate as $Zr_{0.5}Ce_{0.5}O_2$–Al_2O_3. Thus, catalysts supported on Al_2O_3, CeO_2–Al_2O_3 and $Zr_{0.25}Ce_{0.75}O_2$–Al_2O_3 were showed the worst performance. The results are in agreement with those reported in the literature [62]. Thus, a more stable performance was achieved for mixed oxides with zirconium rich compositions than those with cerium rich compositions.

Additionally, it has been widely reported that under reductive conditions the close interaction between CeO_2 and Al_2O_3 might lead to the formation of $CeAlO_3$ [42]. The formation of such a material would have detrimental effects on the of the OSC properties of the ceria [22]. Fig. 11a–c is presenting a comparison of the UV-Raman and XRD results for samples after calcination (calcined) and samples after reduction in H_2 flow at 1173 K for 1 h. UV-Raman spectrum in Fig. 11a for the CeO_2–Al_2O_3 sample was showing a pronounced decrease in the band related with the fluorite structure after reduction (460 cm^{-1}). Additionally, the peak related with the c-CeO_2 for XRD in the 2θ interval between 27 and 32° disappeared for the reducted sample (profile 4) in Fig. 11c, whereas it was clearly observed for the calcined one (profile 3). Besides, UV-Raman spectrum for a $Zr_{0.5}Ce_{0.5}O_2$–Al_2O_3 sample after calcination at 1473 K was compared with the spectrum of the same sample after calcination and reduction in Fig. 11b. Furthermore, XRD profiles were recorded for the sample after calcination at 1173 K for 5 h and reduction at 1173 K for 1 h, patterns 1 and 2 in Fig. 11c, respectively. The obtained profiles before and after reduction were almost coincident for both techniques, thus confirming the absence of the cerium aluminate in this case. Summarizing, the combination of the earlier formation of the α-phase with the $CeAlO_3$ might be responsible of the worse stability observed for catalysts supported on CeO_2–Al_2O_3.when compared with $Zr_{0.5}Ce_{0.5}O_2$–Al_2O_3.

4. Conclusions

Alumina based nanocomposites were synthesized through a citrate mediated route. Cerium and zirconium nitrates were employed for modifying the alumina support. Highly dispersed $Zr_xCe_{1-x}O_2$ on the surface of Al_2O_3 retarded the phase transformation of Al_2O_3. Low contents of $Zr_xCe_{1-x}O_2$ were sufficient to enhance the thermal stability of alumina. Mixed oxides (*i.e.* $Zr_{0.5}Ce_{0.5}O_2$ or $Zr_{0.25}Ce_{0.75}O_2$) were found to be more effective in improving the thermal stability of the alumina support than the single ceria or zirconia. Thus, the complete transformation to α-alumina was found for those catalyst after treatments at 1473 K, whereas a mixture of the α- and θ-phases is obtained for the mixed systems.

As GHSV increases, methane conversion and selectivity to synthesis gas increases. Increased methane conversion means higher energy input and therefore higher temperatures, which favor synthesis gas production. Subsequently, it can be concluded that the system operates under transport controlled regime.

The partial oxidation of methane was studied for Rh catalysts supported on $Zr_{0.25}Ce_{0.75}O_2$–Al_2O_3, $Zr_{0.5}Ce_{0.5}O_2$–Al_2O_3,

ZrO_2–Al_2O_3, CeO_2–Al_2O_3 and Al_2O_3. For a stoichiometric CH_4–air mixture, zirconia on alumina supported catalysts showed a worse catalytic performance than zirconia/ceria-promoted catalysts. Catalysts supported on CeO_2–Al_2O_3 and $Zr_{0.5}Ce_{0.5}O_2$–Al_2O_3 showed the best behavior probably due to the slightly higher rhodium dispersion as well as the properties of ceria for promoting the water gas shift reaction and the oxygen mobility. The ignition–extinction behavior for Rh supported catalysts was also studied. A clear dependence was found with the Rh loading, thus, the lower amount of Rh provokes a delay in the ignition. The combustion of methane was found to be more favorable over Rh supported on ZrO_2–Al_2O_3, whereas steam reforming was promoted on the Ce-based catalysts due to the slightly higher dispersion. Additionally, catalysts supported on $Zr_{0.5}Ce_{0.5}O_2$–Al_2O_3 showed the most stable performance after testing during 42 h. The formation of the $CeAlO_3$ for the rich ceria composition might contribute to the deactivation. Summarizing, it can be concluded that the composition of the support has an important effect in the partial oxidation of methane to produce synthesis gas over Rh-based catalysts.

Acknowledgements

The financial support from the Norwegian Research Council and Statoil is greatly acknowledged.

References

[1] B.C. Enger, R. Lødeng, A. Holmen, Applied Catalysis A: General 346 (2008) 1.
[2] L. Pino, V. Recupero, S. Beninati, A.K. Shukla, M.S. Hegde, P. Bera, Applied Catalysis A: General 225 (2002) 63.
[3] B.C. Enger, R. Lødeng, A. Holmen, Applied Catalysis A: General 364 (2009) 15.
[4] B.C. Enger, R. Lødeng, A. Holmen, Journal of Catalysis 262 (2009) 188.
[5] P.P. Silva, F.A. Silva, H.P. Souza, A.G. Lobo, L.V. Mattos, F.B. Noronha, C.E. Hori, Catalysis Today 101 (2005) 31.
[6] J.-D. Grunwaldt, S. Hannemann, C.G. Schroer, A. Baiker, The Journal of Physical Chemistry B 110 (2006) 8674.
[7] R. Lanza, S.G. Järås, P. Canu, Applied Catalysis A: General 325 (2007) 57.
[8] A. Donazzi, B.C. Michael, L.D. Schmidt, Journal of Catalysis 260 (2008) 270.
[9] M. Bizzi, L. Basini, G. Saracco, V. Specchia, Chemical Engineering Journal 90 (2002) 97.
[10] S. Hannemann, J.-D. Grunwaldt, B. Kimmerle, A. Baiker, P. Boye, C. Schroer, Topics in Catalysis 52 (2009) 1360.
[11] M. Ozawa, M. Kimura, A. Isogai, Journal of the Less Common Metals 162 (1990) 297.
[12] X. Wu, B. Yang, D. Weng, Journal of Alloys and Compounds 376 (2004) 241.
[13] Y. Jia, Y. Hotta, K. Sato, K. Watari, Journal of the American Ceramic Society 89 (2006) 1103.
[14] R. Di Monte, P. Fornasiero, J. Kaspar, M. Graziani, J.M. Gatica, S. Bernal, A. Gómez-Herrero, Chemical Communications (2000) 2167.
[15] B. Reddy, A. Khan, Catalysis Surveys from Asia 9 (2005) 155.
[16] J. Wang, J. Wen, M. Shen, The Journal of Physical Chemistry C 112 (2008) 5113.
[17] S. Rossignol, C. Kappenstein, International Journal of Inorganic Materials 3 (2001) 51.
[18] A. Vazquez, T. Lopez, R. Gomez, X. Bokhimi, Journal of Molecular Catalysis A: Chemical 167 (2001) 91.
[19] L. De Rogatis, T. Montini, M.F. Casula, P. Fornasiero, Journal of Alloys and Compounds 451 (2008) 516.
[20] R. Di Monte, P. Fornasiero, S. Desinan, J. Kaspar, J.M. Gatica, J.J. Calvino, E. Fonda, Chemistry of Materials 16 (2004) 4273.
[21] R. Di Monte, P. Fornasiero, J. Kaspar, P. Rumori, G. Gubitosa, M. Graziani, Applied Catalysis B: Environmental 24 (2000) 157.
[22] A. Trovarelli, Catalysis by Ceria and Related Materials, World Scientific Publishing Company, London, 2002.
[23] V.B. Mortola, J.A.C. Ruiz, L.V. Mattos, F.B. Noronha, C.E. Hori, Catalysis Today 133–135 (2008) 906.
[24] F.d.A. Silva, J.A.C. Ruiz, K.R. de Souza, J.M.C. Bueno, L.V. Mattos, F.B. Noronha, C.E. Hori, Applied Catalysis A: General 364 (2009) 122.
[25] P.P. Silva, F.A. Silva, L.S. Portela, L.V. Mattos, F.B. Noronha, C.E. Hori, Catalysis Today 107–108 (2005) 734.
[26] T. Zhao, S. Boullosa-Eiras, Y. Yu, D. Chen, A. Holmen, M. Rønning, Topics in Catalysis, doi:10.1007/s11244-011-9738-2, in press.
[27] H.M. Rietveld, Journal of Applied Crystallography 2 (1969) 65.
[28] G.S. Pawley, Journal of Applied Crystallography 14 (1981) 357.
[29] E. Smith, G. Dent, Modern Raman Spectroscopy: A Practical Approach, Wiley and Sons, England, 2008.
[30] J.M. Gatica, R.T. Baker, P. Fornasiero, S. Bernal, G. Blanco, J. Kaspar, The Journal of Physical Chemistry B 104 (2000) 4667.
[31] J.M. Gatica, R.T. Baker, P. Fornasiero, S. Bernal, J. Kaspar, The Journal of Physical Chemistry B 105 (2001) 1191.
[32] P.A. Badkar, J.E. Bailey, Journal of Materials Science 11 (1976) 1794.
[33] S. Boullosa-Eiras, E. Vanhaecke, T. Zhao, D. Chen, A. Holmen, Catalysis Today 166 (2011) 10.
[34] A.E. McHale, Phase diagrams for ceramists, in: Proceedings of the Annual 1991, 1991.
[35] C. Li, M. Li, Journal of Raman Spectroscopy 33 (2002) 301.
[36] M. Li, Z. Feng, G. Xiong, P. Ying, Q. Xin, C. Li, The Journal of Physical Chemistry B 105 (2001) 8107.
[37] B. Reddy, P. Saikia, P. Bharali, Catalysis Surveys from Asia 12 (2008) 214.
[38] L. Li, Y. Zhan, Q. Zheng, Y. Zheng, C. Chen, Y. She, X. Lin, K. Wei, Catalysis Letters 130 (2009) 532.
[39] A. Martinez-Arias, M. Fernandez-Garcia, L.N. Salamanca, R.X. Valenzuela, J.C. Conesa, J. Soria, The Journal of Physical Chemistry B 104 (2000) 4038.
[40] Z.V. Popovic, Z. Dohcevic-Mitrovic, A. Cros, A. Cantarero, Journal of Physics: Condensed Matter (2007) 496209.
[41] B.M. Reddy, K.N. Rao, G.K. Reddy, A. Khan, S.-E. Park, The Journal of Physical Chemistry C 111 (2007) 18751.
[42] J.Z. Shyu, W.H. Weber, H.S. Gandhi, The Journal of Physical Chemistry 92 (2002) 4964.
[43] J.E. Spanier, R.D. Robinson, F. Zhang, S.-W. Chan, I.P. Herman, Physical Review B 64 (2001) 245407.
[44] T. Taniguchi, T. Watanabe, N. Sugiyama, A.K. Subramani, H. Wagata, N. Matsushita, M. Yoshimura, The Journal of Physical Chemistry C 113 (2009) 19789.
[45] A. Cabanas, J.A. Darr, E. Lester, M. Poliakoff, Journal of Material Chemistry 11 (2001) 561.
[46] N. Gavrilova, O. Zhilina, V. Nazarov, Russian Journal of Applied Chemistry 80 (2007) 1468.
[47] K. Nakano, T. Masui, G.-y. Adachi, Journal of Alloys and Compounds 344 (2002) 342.
[48] P. Fornasiero, J. Kaspar, T. Montini, M. Graziani, V. Dal Santo, R. Psaro, S. Recchia, Journal of Molecular Catalysis A: Chemical 204–205 (2003) 683.
[49] R. Horn, K.A. Williams, N.J. Degenstein, A. Bitsch-Larsen, D. Dalle Nogare, S.A. Tupy, L.D. Schmidt, Journal of Catalysis 249 (2007) 380.
[50] J.J. Spivey, Catalysis, The Royal Society of Chemistry, 2000.
[51] S.C. Tsang, J.B. Claridge, M.L.H. Green, Catalysis Today 23 (1995) 3.
[52] M. Maestri, A. Beretta, G. Groppi, E. Tronconi, P. Forzatti, Catalysis Today 105 (2005) 709.
[53] J.-D. Grunwaldt, L. Basini, B.S. Clausen, Journal of Catalysis 200 (2001) 321.
[54] J.-D. Grunwaldt, Journal of Physics: Conference Series 190 (2009) 012151.
[55] S. Eriksson, S. Rojas, M. Boutonnet, J.L.G. Fierro, Applied Catalysis A: General 326 (2007) 8.
[56] Y. Madier, C. Descorme, A.M. Le Govic, D. Duprez, The Journal of Physical Chemistry B 103 (1999) 10999.
[57] B.C. Enger, Hydrogen production by catalytic partial oxidation of methane, Ph.D. Thesis, NTNU, Trondheim, 2008.
[58] H.S. Fogler, Elements of chemical reaction engineering, Person international edition, Massachusetts, 2005.
[59] J. Wei, E. Iglesia, Journal of Catalysis 225 (2004) 116.
[60] J.H. Lee, D.L. Trimm, Fuel Processing Technology 42 (1995) 339.
[61] J.C. Mackie, Catalysis Reviews: Science and Engineering 33 (1991) 169.
[62] Z. Yuan, C. Ni, C. Zhang, D. Gao, S. Wang, Y. Xie, A. Okada, Catalysis Today 146 (2009) 124.